ADVANCED MATERIALS
www.advmat.de

3D Printed High-Performance Lithium Metal Microbatteries Enabled by Nanocellulose

Daxian Cao, Yingjie Xing, Karnpiwat Tantratian, Xiao Wang, Yi Ma, Alolika Mukhopadhyay, Zheng Cheng, Qing Zhang, Yucong Jiao, Lei Chen, and Hongli Zhu**

Batteries constructed via 3D printing techniques have inherent advantages including opportunities for miniaturization, autonomous shaping, and controllable structural prototyping. However, 3D-printed lithium metal batteries (LMBs) have not yet been reported due to the difficulties of printing lithium (Li) metal. Here, for the first time, high-performance LMBs are fabricated through a 3D printing technique using cellulose nanofiber (CNF), which is one of the most earth-abundant biopolymers. The unique shear thinning properties of CNF gel enables the printing of a $LiFePO_4$ electrode and stable scaffold for Li. The printability of the CNF gel is also investigated theoretically. Moreover, the porous structure of the CNF scaffold also helps to improve ion accessibility and decreases the local current density of Li anode. Thus, dendrite formation due to uneven Li plating/stripping is suppressed. A multiscale computational approach integrating first-principle density function theory and a phase-field model is performed and reveals that the porous structures have more uniform Li deposition. Consequently, a full cell built with a 3D-printed Li anode and a $LiFePO_4$ cathode exhibits a high capacity of 80 mA h g^{-1} at a charge/discharge rate of 10 C with capacity retention of 85% even after 3000 cycles.

3D printing, also known as additive manufacturing, creates 3D products by laying down successive layers based on digital programming. This technique is featured by its versatility and accuracy, and more importantly, it can produce complex shapes with less material cost than traditional manufacturing.[1] It has been widely used to make functional devices in numerous fields, such as biomedicine,[2] electronics,[3] engineered composites,[4] microfluidics,[5] and energy storage systems.[6] High viscosity and shear-thinning are desired properties for the inks used for printing to achieve a high-quality product.[7] Most commonly used inks for printing, metal and fossil oil-derived plastics, are scarce and not renewable. In addition, a high temperature is required for these materials since they are used in their molten state that makes the manufacturing process more tedious and energy consuming. Therefore, there is a need to develop low-cost and novel inks, which is abundant in nature and can be printed at room temperature.[8]

Cellulose nanofibers (CNFs) are the ideal candidate for 3D printing inks owing to the combination of natural abundance and the unique properties of the aqueous solution of CNFs.[9] First, the rich hydroxyl groups on each cellulose molecule (six in each repeat unit) form strong hydrogen bonding between individual fibers, as well as with water molecules, when CNFs are dissolved in water. This strong hydrogen bonding promotes high water retention (as high as 98%) and also endows unique viscoelastic performance.[10] Second, CNF acts as a surfactant to assist various other materials dispersed in aqueous solution due to its extremely high negative zeta potential (≈60 mV).[11] Owing to these two properties, CNF can be used as a viscosifier to enable printability of other materials. Third, the nanocellulose has a high Young's Modulus of ≈145–150 GPa,[12] which is beneficial for maintaining the structural integrity after removal of water as a scaffold material.

To the best of our knowledge, CNF has not been applied to 3D printing technology in the fabrication of lithium metal batteries (LMBs). LMBs are regarded as the holy grail of next-generation energy storage due to the high-energy density of Li metal and low standard reduction potential (−3.04 V versus standard hydrogen electrode).[13] However, most of Li electrodes are used in the form of planar metal, which restricts the possibilities for miniaturization and autonomous shaping to be well compatible with the integrated circuit.[14] On top of that, it is undeniable that the fabrication of Li metal through 3D printing is not quite viable, as Li metal is highly reactive and exists in a solid state at room temperature.[15] So far, the representative works on 3D printed batteries were all based on the Li-ion batteries (LIBs) without using Li metal, and the inks consisted of electrode active materials and viscosifier.[16] In this work, for the first time, we successfully fabricated the LMBs through 3D printing method,

D. Cao, Y. Xing, Y. Ma, A. Mukhopadhyay, Z. Cheng, Dr. Q. Zhang, Dr. Y. Jiao, Dr. H. Zhu
Department of Mechanical and Industrial Engineering
Northeastern University
360 Huntington Avenue, Boston, MA 02115, USA
E-mail: h.zhu@neu.edu
K. Tantratian, X. Wang, Dr. L. Chen
Mechanical Engineering Department
Mississippi State University
224 Carpenter building, Mississippi State, MS 39762, USA
E-mail: chen@me.msstate.edu

DOI: 10.1002/adma.201807313

where the CNF-based inks were utilized as the surfactant and viscosifier for the $LiFePO_4$ (LFP) cathode and multifunctional scaffold for the Li anode, respectively. Moreover, without any conductive additives, the electrical conductivity of the electrode was significantly improved by the carbonization of CNF (c-CNF).

Herein, we adopted a two-step approach to prepare the Li anode. A scaffold of CNF was 3D printed into the designed structure, and then Li metal was infused into the carbonized scaffold to form the anode with a high-aspect ratio (c-CNF/Li). With a porous structure, the c-CNF/Li anode can effectively stabilize Li and suppress the dendrite by decreasing local current density and enhancing ion accessibility.[17] In the cathode part, LFP electrode (c-CNF/LFP) was successfully printed using the CNF-based ink. Our design strategies shed light on advanced manufacturing of LMBs, especially microbatteries in particular. We also believe that our work will inspire a variety of practical applications with sustainable and cost-effective materials.

The goal of this work is to use CNF-based inks to enable the LMBs through 3D printing method. The origin of CNF and the design features of our LMBs were schematically illustrated in **Scheme 1**. CNF is easily obtained by disintegrating the wood microfibers derived from trees with a 2,2,6,6-tetramethylpiperidine-1-oxyl (TEMPO) mediated oxidation treatment (Scheme 1a and Figure S1, Supporting Information).[18] Individual fibers of CNF are bonded together by strong hydrogen bonding, which is the reason of the CNF gel has a high viscosity and shear-thinning property. Utilizing CNF-based inks, both the cathode (c-CNF/LFP) and the anode (c-CNF/Li) was printed into a 3D interdigitated structure with high-aspect ratios, as presented in Scheme 1b. In the composite cathode, as shown in Scheme 1c, the LFP particles were percolated by c-CNF to ensure the integrity of the electrode. Further, the percolation of c-CNF can enhance the electrical conductivity of the electrode. Note that there are no other conductive additives like carbon black in the electrode. In the Li metal anode, as shown in Scheme 1d, the c-CNF scaffold was mechanically robust to tolerate the extreme conditions for Li infusion. Furthermore, due to the high water retention, both cathode and anode possess porous structure after the removal of water, which endowed high ion accessibility to the electrodes. As we designed, the porous c-CNF scaffold not only enabled the 3D structure of Li with high-aspect ratio, but also promoted the electrolyte accessibility, reduced local current density, and accommodated the Li volume expansion during the plating process, which could effectively suppress the dendrite formation.

Figure 1 displays the rheological properties of different inks and the printing process of the cathode and anode scaffold. Figure 1a shows the photographs of as-prepared pristine CNF gel, CNF ink, CNF/LFP ink, and the aqueous dispersion of LFP stored in vials and placed reversely. All the CNF-containing inks were highly viscous and stuck to the bottom of the vial firmly. In sharp contrast, the LFP dispersion was fluid-like and could not be used as a ink for printing. The pristine CNF gel with a solid content higher than ≈5.0 wt% is opaque. After high-intensity probe sonication, the dimension of the fibers was reduced to nanometer scale (Figure S2, Supporting Information), and more hydroxyl groups were exposed to the surface of the fibers. The additional exposed hydroxyl groups formed stronger hydrogen bonding between fibers and fiber-water interface. The viscosity increased dramatically and the CNF ink became transparent. Eventually, the solid content increased to 8.3 wt.% due to the loss of water in the process of sonication. With the presence of CNF in the ink, LFP powders could be uniformly dispersed, and the CNF/LFP ink showed high viscosity with a solid content of 13.9 wt%.

Using a benchtop robot with three-axes micro-positioning stage controlled by the pre-programmed procedure (Figure S3, Supporting Information), we printed the 3D-structured electrode layer-by-layer on glass slides. The inks were injected from a nozzle at a moderate and constant speed of 2 mm s^{-1} (Video 1 Anode scaffold and Video 2 Cathode electrode). Figure 1b displays the filaments of CNF/LFP extruded from the 150 µm nozzle. As shown in Figure 1c, the anode scaffold containing 21 layers, where the adjacent layers tightly adhered to each other, was printed with CNF ink and the structure can very well retain its integrity. After freeze-drying, the CNF/LFP samples with 9, 12, 15, and 21 layers are shown in Figure 1d. The desired structure after drying was well maintained, and the height increased with increasing number of layers. To understand the

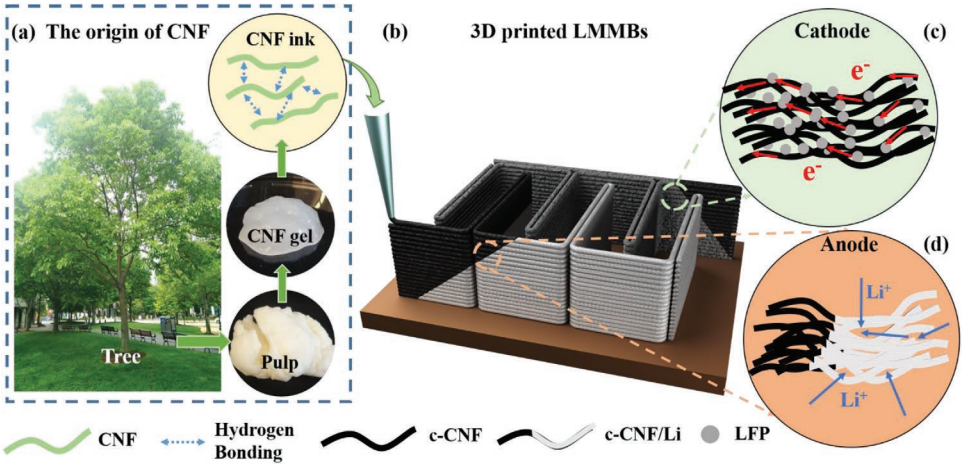

Scheme 1. Schematic representation of a) the CNF ink derived from trees; b) 3D printed LMBs with high-aspect ratio; c) the c-CNF/LFP cathode showing that the LFP particles linked with c-CNF; and d) the 3D printed c-CNF working as a stable and robust scaffold to host Li.

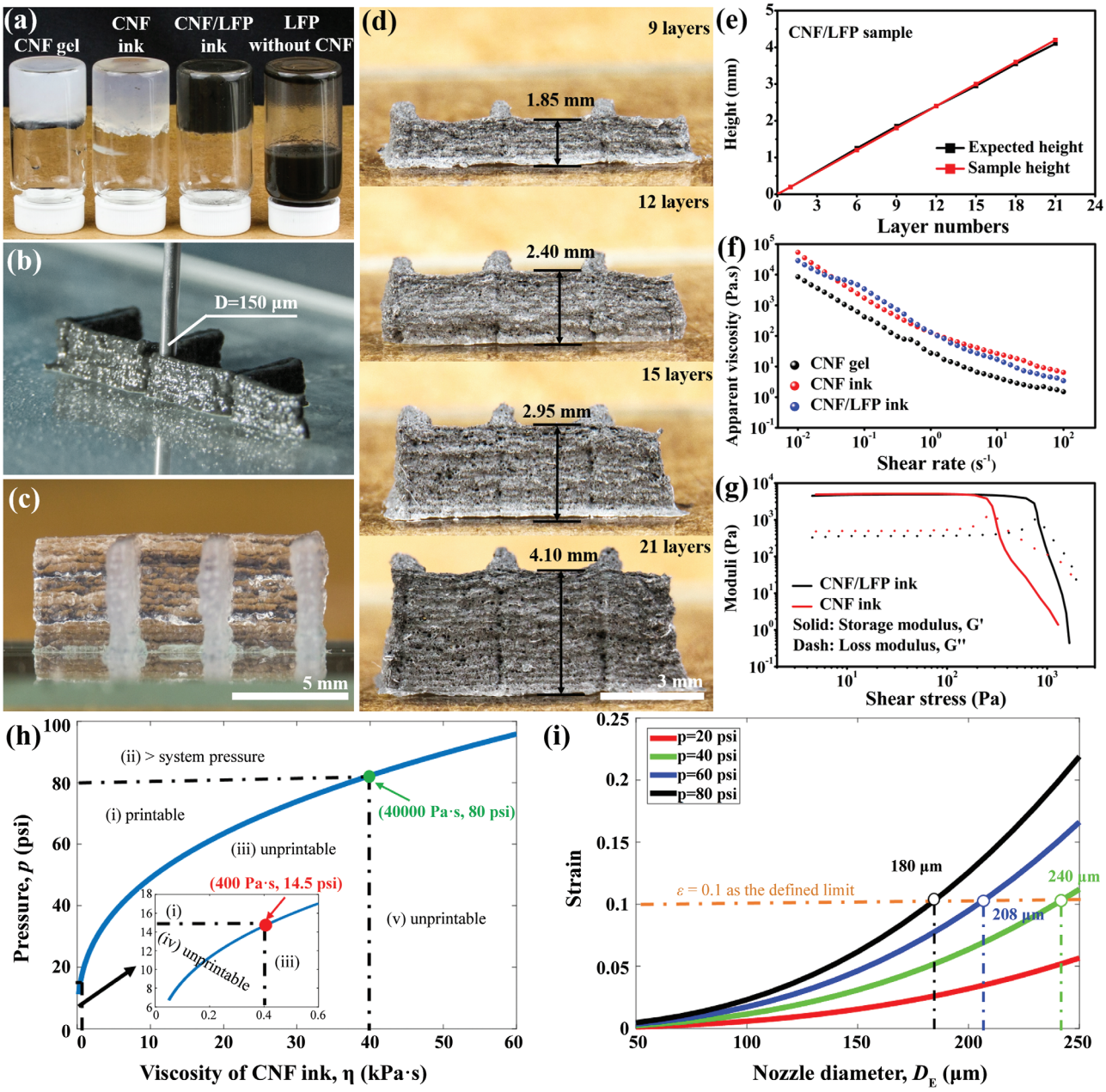

Figure 1. The rheological properties of the inks and digital images to show the printing process. Digital image of a) pristine CNF gel, CNF ink, CNF/LFP ink, and LFP dispersion stored in inverted vials to show viscosity. b) CNF/LFP electrode printed layer by layer. c) Scaffold printed with CNF ink before drying and d) dried CNF/LFP electrode printed with different layers from 9 to 21. e) Expected and real heights of CNF/LFP as a function of layer number. f) Apparent viscosity as a function of shear rate for pristine CNF gel; CNF ink, and CNF/LFP ink. g) The storage modulus, G', and loss modulus, G'', as a function of shear stress for CNF and CNF/LFP inks. h) The required extrusion pressure as a function of the viscosity of CNF ink. i) Strain deformation of the previously deposited layer as a function of the nozzle diameter, D_E, at different extrusion pressures: red line $p = 20$ psi, green line $p = 40$ psi, blue line $p = 60$ psi, and black line $p = 80$ psi.

relationship between the layer numbers and the height of the structure, a comparison of the predicted and the real height of the electrodes as a function of the layer numbers were demonstrated in Figure 1e. One single layer has a thickness of 0.20 mm, and the electrodes with 9, 12, 15, and 21 layers have a thickness of 1.85, 2.40, 2.95, and 4.10 mm, respectively, relating well with the expected heights. A linear relationship was established between the thickness of the electrode and the number of layers.

The well-maintained shape of the electrodes was attributed to the viscoelastic properties of CNF-based inks. Figure 1f compares the viscosity of CNF as a function of shear rate. All three samples behaved as non-Newtonian fluids with similar shear-thinning properties, enabling excellent printability. The pristine CNF gel showed an apparent viscosity ranging from 10 to 10^2 Pa·s at a shear rate of 1 s^{-1}. The viscosity of the CNF ink highly increased after sonication ranging from 10^2 to 10^3 Pa·s at the

shear rate of 1 s^{-1} due to the liberation of nanofibers and formation of more hydrogen bonding. The viscosity curve of CNF/LFP ink overlapped with that of CNF ink, indicating that the addition of LFP has no significant effect on the viscosity of CNF/LFP ink. To evaluate the viscoelastic properties of CNF/LFP and CNF inks, an oscillatory measurement was performed to measure the storage modulus (G') and loss modulus (G'') at low strains, and the results are shown in Figure 1g. For both inks, the plateaus of storage modulus were located between 10^3 and 10^4 Pa, which is one order of magnitude higher than that of loss modulus. The predominant elastic behavior ($G' > G''$) further verifies the solid-like nature of these inks. Meanwhile, the well-defined shear yield stress ($G'' = G'$) was in the range of 10^2–10^3 Pa. These data evidence the structural robustness of the CNF inks. To demonstrate the structural robustness, other structures such as spiral cylinders and squares were also printed, as shown in Figure S4 in the Supporting Information.

Theoretical analysis was then conducted to quantify the printability of CNF ink at various printing parameters. To successfully printing CNF ink, it has to maintain a stable geometry (usually a rectangular shape) once the bead of CNF-ink extruded and created. At a conservative estimate, the extruded material must support the entire weight of the deposited bead throughout a characteristic processing time. Based on Maxwell model,[19] a minimum viscosity should be met to retain the geometry at the following parameters, such as the nozzle moving velocity, the distance between the substrate and the nozzle, and the layer height and width, etc. On the other hand, printing CNF ink at a given viscosity requires a minimum pressure to extrude the viscoelastic fluid at a desired volume flow rate.[4] Figure 1h shows the necessary printing pressure as a function of the viscosity of CNF ink, in which the plot can be divided into five regions. Combining Maxwell model and our experiment inputs yields the minimum required viscosity is 400 Pa·s that further require the extrusion pressure larger than 14.5 psi (≈100 kPa). In our system, since the maximum system pressure is 80 psi (≈551 kPa), the maximum extrudable viscosity is 40 000 Pa·s (the details are provided in Supporting Information). Thus, only the region (i) is the printable region, in which the viscosity is large enough to hold the weight of deposited bead throughout the characteristic processing time. Also, above the cure line, the extrusion system can successfully extrude CNF ink at the desired flow rate without clogging the nozzle. Meanwhile, a previously deposited layer, acting as a substrate, needs to resist the flow and compassion of the current deposited layer. In this case, the strain deformation of the previously deposited layer (or the substrate layer) must be kept below a defined limit ($\varepsilon < 10\%$) to maintain geometry accuracy. Figure 1i shows the strain, ε, of the previously deposited layer, varying as a function of the nozzle diameter, D_E, at different applied extrusion pressures. Clearly, the strain of the previously deposited layer is proportional to the nozzle diameter. A larger nozzle diameter, D_E, brings more deformation to the substrate layer. It is also observed that increasing extrusion pressure can damage the geometry accuracy of the previously deposited layer.

Figure 2 displays the printed structures and characterizations of the cathode. The printing process was recorded with the digital images shown in Figure S5 in the Supporting Information. After the product was printed out and freeze-dried, annealing at 700 °C was performed to obtain the carbonized CNF/LFP electrode. As shown in Figure 2a, the c-CNF/LFP containing 18 layers maintained the as-printed shape very well even after high-temperature annealing and the adjacent layers were stacked together tightly. Scanning electron microscopy (SEM) was used to investigate the morphology of the printed CNF/LFP electrode. From the cross-sectional view in Figure 2b, the width of the filament was around 220 μm, indicating that the as-printed structure has a high-aspect ratio (h/w, where h is height and w is width) of 16.4. Inside the electrode, the c-CNF gathered into interconnected flakes to form a 3D, cross-linked, and porous structure (Figure 2c) after the removal of water during the freeze-drying process. From the surface view (Figure 2d), the printed c-CNF/LFP has a layered structure, in which each filament has the same height of around 200 μm. Figure 2e depicts the magnified morphology of the boundary, where the adjacent filaments were interconnected through the c-CNF flakes. The LFP particle used here has a diameter varying from 200 to 500 nm (Figure S6, Supporting Information). As revealed in Figure 2f, the LFP particles were homogeneously distributed on the surface of the c-CNF matrix, where the carbonized fibers tightly linked the particles to achieve a good connection.

X-ray diffraction (XRD) was used to confirm the LFP had no phase change while mixing with CNF and during the carbonization process (Figure 2g). All the diffraction peaks of LFP powder and c-CNF/LFP electrode were indexed to the crystalline LFP (JCPDS: No.40-1499). The addition of CNF did not change the crystalline structure of LFP. CNF as a carbon source decomposed after annealing and increased the electrical conductivity of the c-CNF/LFP to 28 S cm^{-1}, while that of pure LFP was 10^{-9} S cm^{-1}.[20] Raman spectra of LFP powder, c-CNF, and c-CNF/LFP electrodes were compared in Figure 2h. In the peaks located at 586, 989, and 1045 cm^{-1} are associated with the intramolecular stretching modes of the PO_4^{3-} groups in LFP.[21] In both the spectra of CNF and c-CNF/LFP, there were two sharp peaks at 1340 and 1589 cm^{-1}, corresponding to the disordered carbon (D peak) and ordered graphite carbon (G peak), respectively.[22] Based on the thermogravimetric analysis (TGA), the weight content of LFP in the printed cathode was around 86.5% (Figure 2i).

To prepare the c-CNF/Li anode, a CNF scaffold was first 3D printed into a designed pattern and then carbonized. The molten Li was infused into the scaffold according to an approach reported in our previous work.[23] The printing process of CNF scaffold is shown in Figure S7 in the Supporting Information. The CNF scaffold with 21 layers remained the desired structure after the removal of water by freeze-drying, as shown in **Figure 3**a. And after carbonization at 700 °C for 2 h, the CNF was still sturdy (Figure 3b). Li was found to be uniformly distributed in the scaffold after the infusion (Figure 3c). Thus, the Li metal with the designed 3D pattern was successfully prepared, and the SEM was used to investigate the morphology. Figure 3d is the surface of the as-printed c-CNF scaffold showing porous and layer-by-layer structure, where the large pores with diameters in micrometer scale are originated from the removal of water during the freeze-drying process. The adjacent filaments were closely connected by the c-CNF flakes at the boundary,

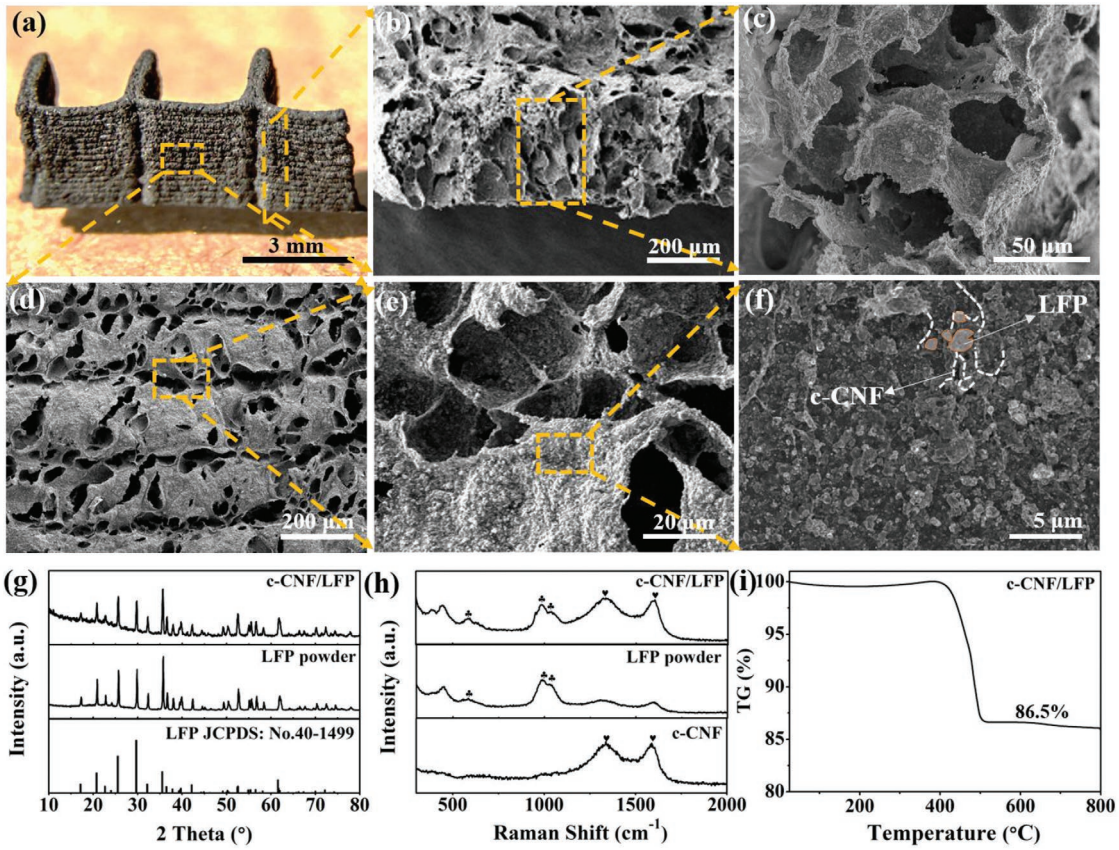

Figure 2. Morphology characterizations, XRD patterns, Raman spectra, and TGA analysis of the cathode part. a) Photographs of c-CNF/LFP electrodes with 18 layers. b) Cross-sectional SEM image of the electrode. c) Cross-sectional SEM of the filament to show the inside morphology of the electrode. d) Surface view of the electrode with layer-by-layer structure. e) SEM image of the boundary between the adjacent filaments. f) SEM image of the electrode. The carbon fiber linking with the LFP particles is highlighted. g) XRD patterns of annealed c-CNF/LFP and LFP powder in comparison with standard peaks. h) Raman spectra of LFP powder, annealed c-CNF/LFP, and CNF. i) TGA curves of the c-CNF/LFP.

which was essential for maintaining the structure well during the melting diffusion process of Li (Figure 3e). In the magnified image, shown in Figure 3f, the pure c-CNF flakes have a very smooth surface. After Li was infused into the c-CNF scaffold, as displayed in Figure 3g, the whole structure was uniformly and continuously covered by the Li. It was interesting that the boundary of the filaments was also covered by Li, which further confirmed the excellent interconnection between the filaments. As shown in Figure 3h, the porous structure was well maintained; the Li covered the surface of the structure without blocking any of the pores. An even Li distribution was also obtained on the surface of c-CNF/Li (Figure 3i).

To investigate the galvanostatic cycling stability of the anode, c-CNF/Li electrode with a planar structure was printed and a symmetric coin cell was assembled (**Figure 4**a). Li foil was used as the anode for the control group. At a high areal current density of 5 mA cm^{-2} and areal charge of 2.5 mAh cm^{-2}, the c-CNF/Li cell showed outstanding stability with a low voltage hysteresis for 300 h. In contrast, the voltage profile of Li foil was stable for 80 h and displayed a gradual increase in hysteresis, which was due to the formation of dendrite and accompanying resistive decomposition species. Figure 4 b–d shows the expansions on the time period of 0–5, 80–85, and 295–300 h of the cycling, respectively. Initially, the c-CNF/Li electrode has a much smaller overpotential (0.05 V) compared to the Li foil (0.38 V), indicating smaller nucleation overpotential (Figure 4b). After cycling for 80 h, the voltage hysteresis of Li foil increased significantly, which was ascribed to higher charge transfer resistance caused by the formation of dendrite (Figure 4c), while there were no changes in the c-CNF/Li electrode. Notably, after plating/stripping for 300 cycles, the c-CNF/Li still showed no increased voltage hysteresis, suggesting a stable Li deposition/dissolution process (Figure 4d). Overall, the c-CNF/Li cell showed a flat plating/stripping plateau with low overpotential (≈0.05 V) throughout the whole cycling process, whereas the Li foil cell exhibited a much higher overpotential (>0.15 V) and gradual hysteresis augment.

To study the suppression of dendrite formation in c-CNF/Li, SEM images were used to compare the morphology of c-CNF/Li and Li foil after cycling for 100 h. Figure 4 e–g revealed the surface morphology of c-CNF/Li at different magnifications. The surface of c-CNF/Li became rougher after cycling for 100 h, compared to its pristine state. Strikingly, no obvious Li dendrites were observed, and the layered and porous structure was well maintained. The SEM observations agreed well with the excellent cycling stability. Compared to c-CNF/Li, severe dendrites were observed in the Li foil electrode after cycling (Figure 4 h–j), which was remarkably different from the

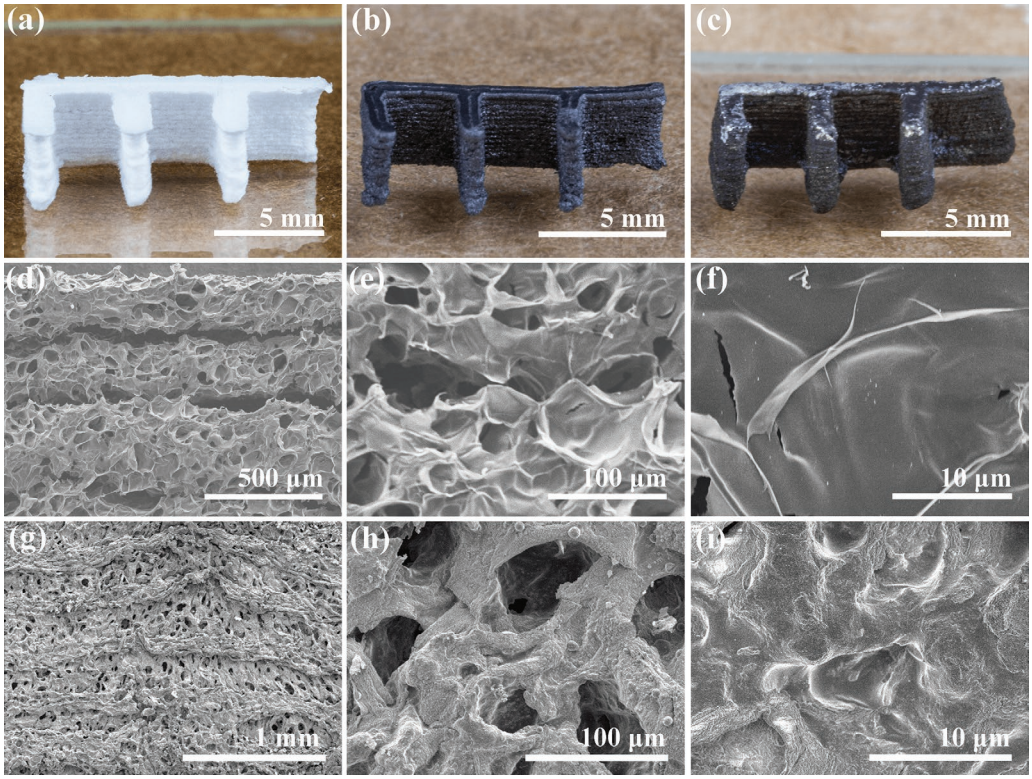

Figure 3. Morphology characterizations of the c-CNF/Li anode before and after being infused with Li. Photographs of a) CNF scaffold after freeze-drying and before carbonization, b) c-CNF scaffold after carbonization, and c) c-CNF/Li electrode with designed 3D structure. d–f) SEM images showing the c-CNF before infusing with Li: d) surface of c-CNF; e) boundary between adjacent layers; and f) surface of c-CNF at a higher magnification. g–i) SEM images of c-CNF/Li after introducing Li: showing g) the surface; h) porous structure; and i) surface of c-CNF/Li at a higher magnification.

flat surface of pristine Li foil (Figure S8, Supporting Information). The observations on Li foil also explains the cycling data. After continuous inhomogeneous deposition/dissolution of Li during cycling, dendrites gradually formed and grew bigger. We believe that the porous structure and high-aspect ratio of the c-CNF/Li can improve the ion transport, reduce the local current density, and accommodate the volume change during the Li plating and stripping. Therefore, the Li dendrite formation is effectively suppressed.

The multiscale computational approach integrating first-principle density function theory (DFT) and phase-field model (PFM) was employed to predict the evolution of Li deposition on the Li metal surface. A solid electrolyte interphase (SEI) layer usually prevents the electron tunneling from the anode but allows Li-ion transport; therefore, Li deposition likely occurs at the Li metal/SEI interface, as illustrated in **Figure 5**a. Typically, the charge transfer reaction involves three main steps: 1) Li-ion desolvation at the SEI/electrolyte interface, 2) Li-ion diffusion through the SEI layer, and 3) reaction at the Li metal/SEI interface. We obtained the energy in each step and the energy landscape of the reaction (Figure 5b) from Li et al.,[24] who employed tight binding or the density functional tight binding method for calculations. The reduced and oxidized state of an Li(001)/Li_2CO_3(001)/EC slab model were considered to estimate the charge transfer reaction energy. It showed the calculated formation energy of the system is 1.42 eV,[24] and this information will be passed to the PFM to predict the microscale Li deposition.

The non-linear PFM accounting for electrochemical reaction kinetics was used to simulate the evolution of Li deposition on 1) the highly porous electrode and 2) Li foil. The simulation details are provided in the Supporting Information. The highly porous c-CNF-Li anode structure with proper Li infusion ensured uniform electrolyte distribution over the electrode surface. Therefore, Li nucleation sites were homogenous, and Li metal grew uniformly on the porous surface, as shown in Figure 5c. However, Li foil was suffered from the massive volumetric change during cycling. This resulted in the cracked SEI layer and thus small perturbations on the electrode surface. Once perturbations were large enough, Li dendrite grew drastically on the Li foil surface, as illustrated in Figure 5f. Figure 5d shows the Li ions evenly distributed near the porous electrode surface, facilitating the uniform Li deposition. In contrast, Figure 5g shows the non-uniform Li-ion concentration near Li foil, suggesting heterogeneous Li deposition on the Li foil surface. Further, Figure 5e displays the uniform local current density near the porous electrode, implying that the Li would continue growing homogeneously out of the electrode surfaces. Whereas, the local current density was highly accumulated only at the dendrite tips for the Li foil, indicating the ongoing development of dendrites, as illustrated in Figure 5h. Additionally, the porous structures also provided mechanical confinement.[25] During platting, Li ions were deposited within the pore and remained confined due to the pore size, which prevents Li dendrite growth.

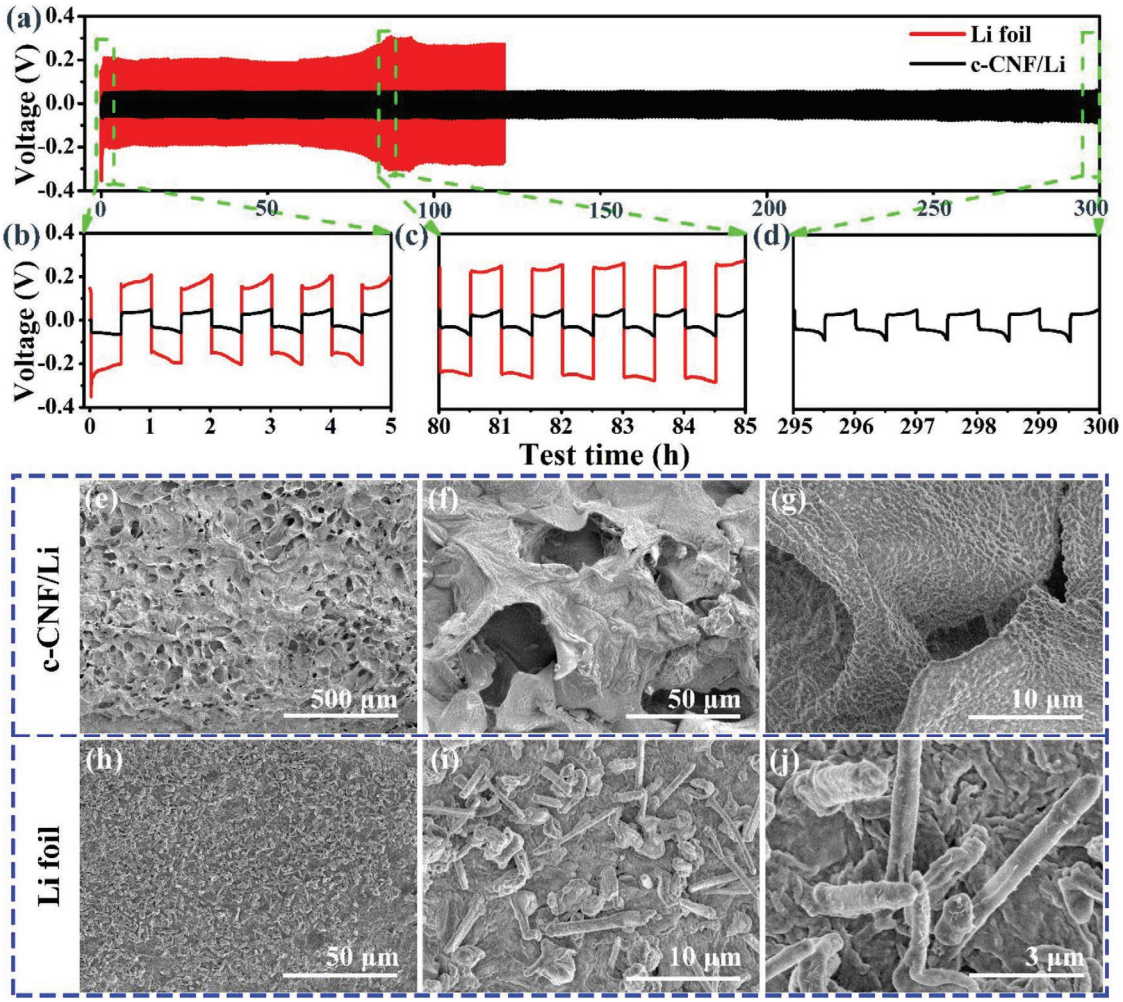

Figure 4. Comparison of c-CNF/Li and Li foil in cycling performance and morphology after cycling. a) Cycling performance in a symmetric cell at the current density of 5 mA cm^{-2} and areal charge of 2.5 mA h cm^{-2}. Expansion of time period b) 0–5 h, c) 80–85 h, and d) 295–300 h. SEM images of c-CNF/Li after cycling showing the e) well-maintained layered structure, f) porous structure, and g) uniform surface with no dendrites formed. SEM images of Li foil after cycling showing h) coarse surface, and i) surface with dendrites formed, and j) dendrites.

Further, to verify the stability, galvanostatic cycling performance of the printed c-CNF/LFP and c-CNF/Li electrodes were also performed, as shown in **Figure 6**. The measurements were conducted on printed planar electrodes (Figure S9, Supporting Information), as detailed in the Experimental Section. The specific capacity of the c-CNF/LFP electrode was calculated based on the mass of active LFP, while the specific capacity of c-CNF/Li electrode was evaluated based on the mass of the electrode including both c-CNF and Li. In the full cell, the current and capacity were calculated according to the mass of the LFP in the cathode. Figure 6a shows the charge/discharge curves of the first two cycles of the c-CNF/LFP half-cell at a rate of 0.2 C (1C = 170 mA g^{-1}). High charge and discharge capacities of 167 and 140 mA h g^{-1}, respectively, were achieved in the first cycle. The relative lower Coulombic efficiency at the first cycle was attributed to the formation of SEI, which is usually seen in porous electrodes. In the subsequent cycles, the charge and discharge capacities were similar, and the cell achieved a high Coulombic efficiency of 97.2%. It is worth mentioning that after one cycle, the voltage hysteresis between the charge and discharge reactions at the second cycle decreased to 0.07 V. The high reaction kinetics was because of the enhanced electrical conductivity of the electrode arising from the presence of c-CNF. For the c-CNF/Li anode, a high-specific capacity of ≈2346 mA h g^{-1} was achieved at the current of 100 mA g^{-1} (Figure 6b), which can be attributed to the light weight of c-CNF. A low overpotential was observed for the c-CNF/Li anode, and the Li stripping took place at around 0.02 V.

Figure 6c shows the charge/discharge curves of the c-CNF/LFP–c-CNF/Li full cell obtained while determining the rate performance. The discharge capacities were 137, 131, 120, 107, 93, and 80 mA h g^{-1} at the discharge rate of 0.2, 0.5, 1, 2, 5, and 10 C, respectively. The corresponding voltage hysteresis were 0.065, 0.09, 0.14, 0.22, 0.38, and 0.66 V, respectively, indicating overall fast reaction kinetics in the full cell. Electrochemical impedance spectroscopy (EIS) measurements were carried out before and after rate performance, and the Nyquist plots are presented in Figure 6d. Initially, the charge transfer resistance, represented by the diameter of the semicircle, was

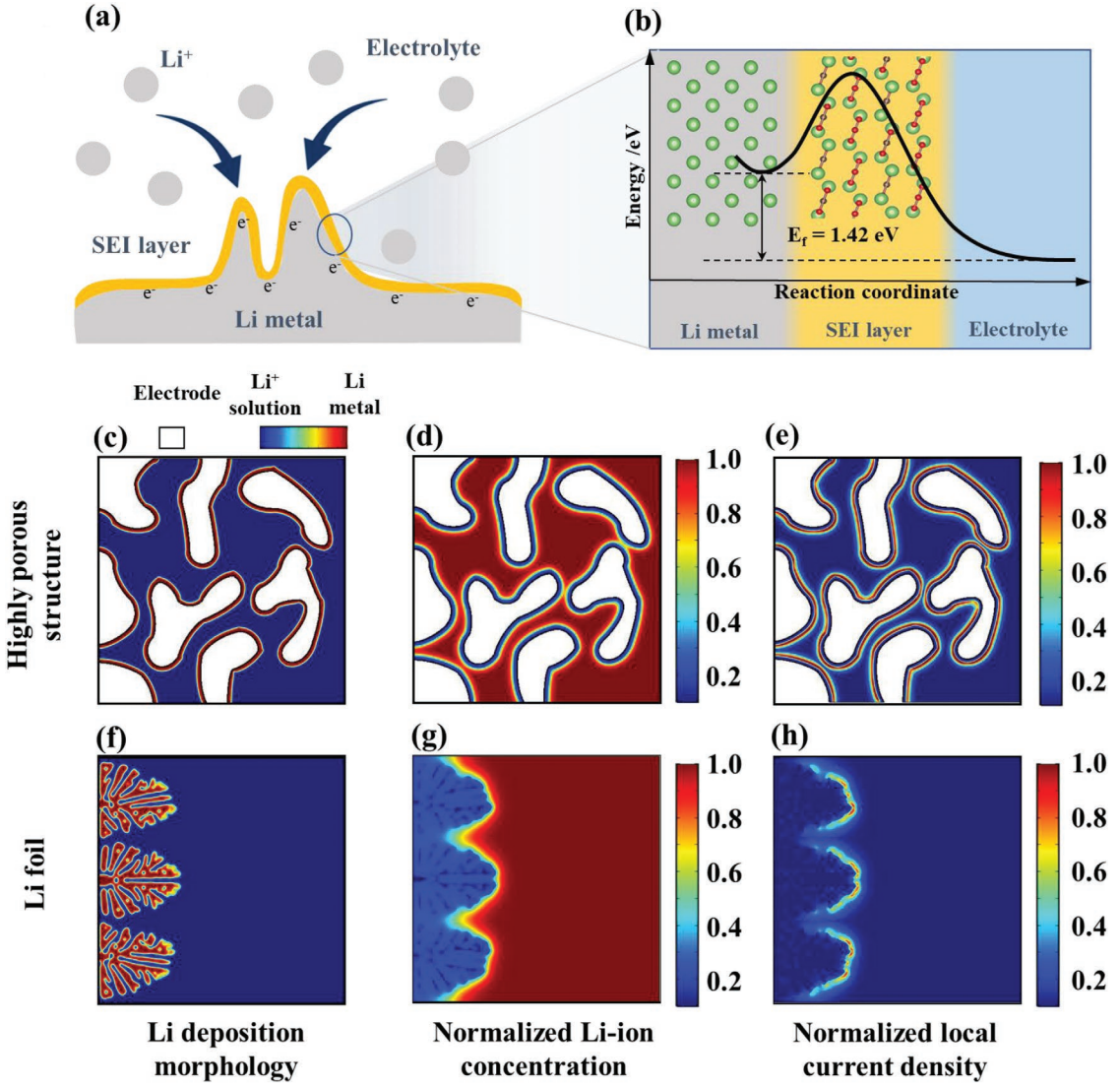

Figure 5. a) Schematic of the Li deposition mechanism. b) Energetic coordinate for the charge transfer reaction at the electrode/SEI/electrolyte interface. The morphology evolution of Li deposition on c) the porous electrode structure and f) Li foil. The Li-ion concentration distributions in the electrolyte near d) the porous electrode structure and g) Li foil. The normalized local current density distributions for e) the porous electrode structure and h) Li foil.

approximately 160 Ω. After the rate performance test was finished, no apparent changes in the semicircle were observed, evidencing high cycling stability of both cathode and anode. The long-term cycling performance of the full cell with printed electrodes is presented in Figure 6e. At a high rate of 10 C, a high discharge capacity of 80 mA h g^{-1} was delivered at the first cycle, and 85% of the initial capacity was maintained even after 3000 cycles. This stable cycling performance of the full cell is ascribed to several factors related to both the cathode and the anode. First, the carbonization of c-CNF drastically improved the electrical conductivity of the composite cathode, and thus enhanced the performance at high rates. Second, the cathode with a 3D porous structure has good accessibility to the electrolyte, which accelerated the charge transfer during cycling. Further, the c-CNF/Li anode can plate and strip Li stably without the issue of dendrite formation.

A planar LMB with printed electrodes was assembled and packaged, and the structure is schematically illustrated in Figure 6f. The as-printed cathode and anode with planar structure were secured onto the Cu and Al foils with Ag paste, respectively. To assemble the cell, polydimethylsiloxane and 5-min epoxy were utilized for preparing the framework and sealing the cell. Cell packaging was performed under argon atmosphere. Figure 6g,h showed that the packaged LMBs could successfully power a white light-emitting diode (LED) lamp with an operating voltage higher than 3.0 V.

Here, for the first time, LMBs fabricated with extrusion-based 3D printing technique with the aid of CNFs were investigated. The printing parameters, including the extrusion pressure and nozzle diameter, has been investigated in experiment and theory. Wood-derived, sustainable, low-cost, and naturally abundant CNF provided excellent printability to the LFP

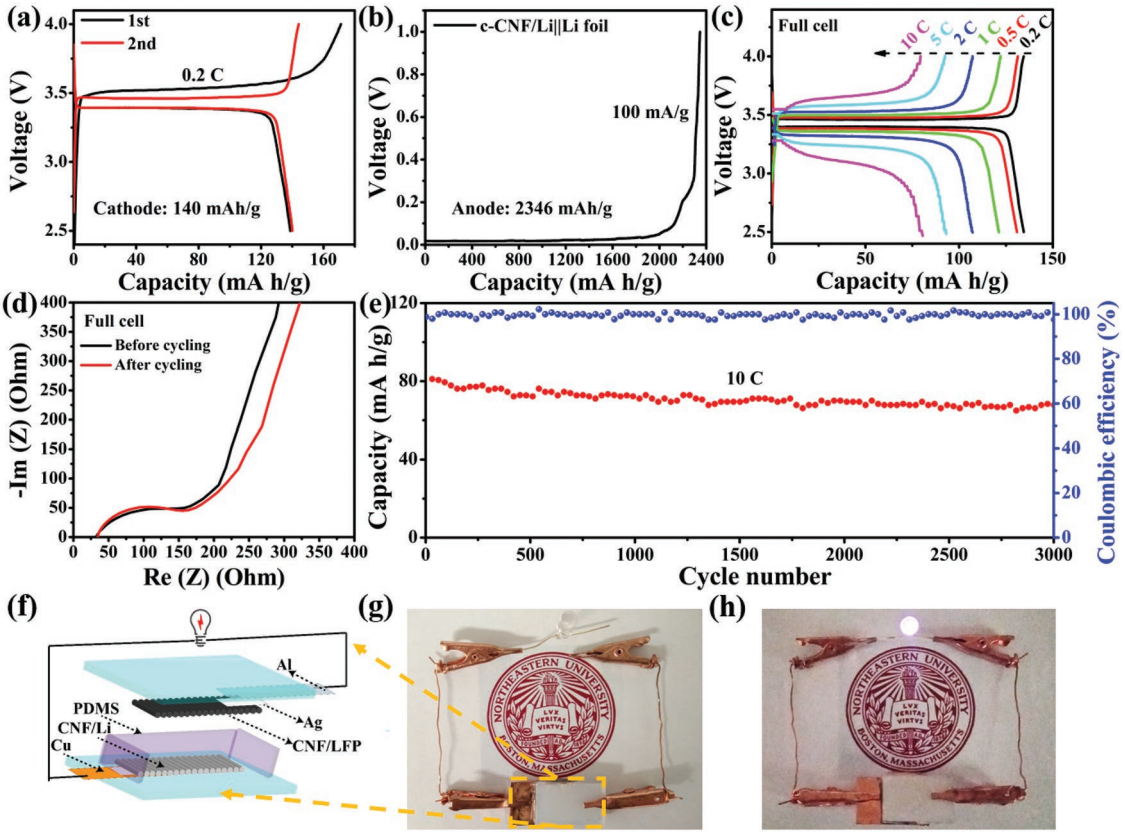

Figure 6. Galvanostatic cycling performance of planner c-CNF/LFP cathode and c-CNF/Li anode and LMBs. a) Charge and discharge profiles of the cell with c-CNF/LFP cathode and Li foil anode at 0.2 C. b) Full Li stripping curve of the c-CNF/Li electrode to 1 V versus Li^+/Li. c) Voltage profiles at various rates from 0.2 to 10 C, d) Nyquist plots of the cell with c-CNF/LFP cathode and c-CNF/Li anode before and after the rate measurement. e) Long-term cycling performance at 10 C for the full cell with c-CNF/LFP cathode and c-CNF/Li anode. f) A schematic to show the cell structure with printed electrodes. The photographs of the packaged LMBs g) before and h) after connecting to power a white LED lamp.

cathode. Meanwhile, the CNF as the scaffold for Li metal anode showed highly stable performance. In the stability test, the c-CNF/Li anode showed a low overpotential of 50 mV and highly stable cycling for 300 cycles at a high current density of 5 $mA \cdot cm^{-2}$. CNF played vital roles in this work: 1) the rich hydroxyl groups, high viscosity, and distinct shear-thinning behavior of CNF-based ink at low concentration rendered CNF as ideal viscosifier; 2) the high negative zeta potential enabled CNF to be an effective surfactant to uniformly disperse the LFP; 3) as a carbon source, CNF after carbonization provided the electrical conductivity of the composite cathode and consequently enhanced the rate performance; 4) the high mechanical strength prevented the structure from collapsing during the freeze-drying process and melting diffusion process of Li; 5) due to a water retention of 92%, a porous aerogel with superior ion accessibility worked as an excellent Li host and effectively suppressed Li dendrite. Furthermore, the multiscale computational approach integrating the first-principle DFT and PFM was performed to confirm that the Li with porous structure can effectively stabilize the Li and suppress the dendrite formation. On the other hand, this printed cathode delivered a high specific capacity of 140 mA h g^{-1} at 0.2 C. When the c-CNF/LFP cathode and the c-CNF/Li anode were tested in full cell, a high specific capacity of 80 mA h g^{-1} was achieved with a capacity retention of 85% after 3000 cycles at 10 C. The 3D-printed LMBs enabled by the CNF are highlighted with their excellent ion accessibility and diverse design.

Supporting Information

The supporting Information is available from the Wiley Online Library or from the author.

Acknowledgements

D.C., Y.X. and K.T. contributed equally to this work. The authors acknowledge the financial support from Northeastern University and Rogers Corporation. The authors also acknowledge the use of XRD, Raman, and TGA facilities under the auspices of the Northeastern University Center for Renewable Energy Technology (NUCRET). The authors thank Dr. Steve Lustig and Artem Isakov in Chemical Engineering at Northeastern University for the help on rheometer measurement. K.T., X.W., and L.C. are grateful for the financial support by NSF-CBET-1604104. The computer simulations were carried out on the clusters of High Performance Computing Collaboratory (HPC^2) at Mississippi State University.

Conflict of Interest

The authors declare no conflict of interest.

Keywords

3D printing, cellulose nanofibers, dendrite, electrical conductivity, lithium metal batteries, viscosifier

Received: November 11, 2018
Revised: January 28, 2019
Published online:

[1] B. Berman, *Bus. Horiz.* **2012**, *55*, 155.
[2] a) S. V. Murphy, A. Atala, *Nat. Biotechnol.* **2014**, *32*, 773; b) D. B. Kolesky, R. L. Truby, A. S. Gladman, T. A. Busbee, K. A. Homan, J. A. Lewis, *Adv. Mater.* **2014**, *26*, 3124.
[3] a) J. T. Muth, D. M. Vogt, R. L. Truby, Y. Mengüç, D. B. Kolesky, R. J. Wood, J. A. Lewis, *Adv. Mater.* **2014**, *26*, 6307; b) J. A. Lewis, B. Y. Ahn, *Nature* **2015**, *518*, 42; c) A. D. Valentine, T. A. Busbee, J. W. Boley, J. R. Raney, A. Chortos, A. Kotikian, J. D. Berrigan, M. F. Durstock, J. A. Lewis, *Adv. Mater.* **2017**, *29*, 1703817.
[4] a) Z. C. Eckel, C. Y. Zhou, J. H. Martin, A. J. Jacobsen, W. B. Carter, T. A. Schaedler, *Science* **2016**, *351*, 58; b) N. W. Bartlett, M. T. Tolley, J. T. B. Overvelde, J. C. Weaver, B. Mosadegh, K. Bertoldi, G. M. Whitesides, R. J. Wood, *Science* **2015**, *349*, 161.
[5] a) S. Waheed, J. M. Cabot, N. P. Macdonald, T. Lewis, R. M. Guijt, B. Paull, M. C. Breadmore, *Lab Chip* **2016**, *16*, 1993; b) A. K. Au, W. Huynh, L. F. Horowitz, A. Folch, *Angew. Chem., Int. Ed.* **2016**, *55*, 3862.
[6] a) K. Fu, Y. G. Yao, J. Q. Dai, L. B. Hu, *Adv. Mater.* **2017**, *29*, 1603486; b) X. Tian, J. Jin, S. Yuan, C. K. Chua, S. B. Tor, K. Zhou, *Adv. Energy Mater.* **2017**, *7*, 1700127.
[7] a) A. Ambrosi, M. Pumera, *Chem. Soc. Rev.* **2016**, *45*, 2740; b) S. Hong, D. Sycks, H. F. Chan, S. Lin, G. P. Lopez, F. Guilak, K. W. Leong, X. Zhao, *Adv. Mater.* **2015**, *27*, 4035.
[8] a) K. M. O. Håkansson, I. C. Henriksson, C. d. l. P. Vázquez, V. Kuzmenko, K. Markstedt, P. Enoksson, P. Gatenholm, *Adv. Mater. Tech.* **2016**, *1*, 1600096; b) V. C.-F. Li, C. K. Dunn, Z. Zhang, Y. Deng, H. J. Qi, *Sci. Rep.* **2017**, *7*, 8018.
[9] a) Y. Li, H. Zhu, Y. Wang, U. Ray, S. Zhu, J. Dai, C. Chen, K. Fu, S. H. Jang, D. Henderson, T. Li, L. Hu, *Small Methods* **2017**, *1*, 1700222; b) S. Shin, J. Hyun, *ACS Appl. Mater. Interfaces* **2017**, *9*, 26438.
[10] a) H. Zhu, S. Zhu, Z. Jia, S. Parvinian, Y. Li, O. Vaaland, L. Hu, T. Li, *Proc. Natl. Acad. Sci. USA* **2015**, *112*, 8971; b) H. Zhu, Y. Li, Z. Fang, J. Xu, F. Cao, J. Wan, C. Preston, B. Yang, L. Hu, *ACS Nano* **2014**, *8*, 3606; c) H. Zhu, W. Luo, P. N. Ciesielski, Z. Fang, J. Y. Zhu, G. Henriksson, M. E. Himmel, L. Hu, *Chem. Rev.* **2016**, *116*, 9305.
[11] a) Y. Kuang, C. Chen, G. Pastel, Y. Li, J. Song, R. Mi, W. Kong, B. Liu, Y. Jiang, K. Yang, L. Hu, *Adv. Energy Mater.* **2018**, *8*, 1802398; b) Y. Li, H. Zhu, F. Shen, J. Wan, S. Lacey, Z. Fang, H. Dai, L. Hu, *Nano Energy* **2015**, *13*, 346.
[12] a) S. Iwamoto, W. Kai, A. Isogai, T. Iwata, *Biomacromolecules* **2009**, *10*, 2571; b) L. Yang, A. Mukhopadhyay, Y. Jiao, Q. Yong, L. Chen, Y. Xing, J. Hamel, H. Zhu, *Nanoscale* **2017**, *9*, 11452.
[13] a) P. Albertus, S. Babinec, S. Litzelman, A. Newman, *Nat. Energy* **2018**, *3*, 16; b) D. Lin, Y. Liu, Y. Cui, *Nat. Nanotechnol.* **2017**, *12*, 194.
[14] a) S. Ferrari, M. Loveridge, S. D. Beattie, M. Jahn, R. J. Dashwood, R. Bhagat, *J. Power Sources* **2015**, *286*, 25; b) S.-H. Kim, K.-H. Choi, S.-J. Cho, S. Choi, S. Park, S.-Y. Lee, *Nano Lett.* **2015**, *15*, 5168.
[15] C. Ladd, J. H. So, J. Muth, M. D. Dickey, *Adv. Mater.* **2013**, *25*, 5081.
[16] a) K. Sun, T. S. Wei, B. Y. Ahn, J. Y. Seo, S. J. Dillon, J. A. Lewis, *Adv. Mater.* **2013**, *25*, 4539; b) K. Fu, Y. B. Wang, C. Y. Yan, Y. G. Yao, Y. A. Chen, J. Q. Dai, S. Lacey, Y. B. Wang, J. Y. Wan, T. Li, Z. Y. Wang, Y. Xu, L. B. Hu, *Adv. Mater.* **2016**, *28*, 2587; c) Y. Wang, C. Chen, H. Xie, T. Gao, Y. Yao, G. Pastel, X. Han, Y. Li, J. Zhao, K. Fu, L. Hu, *Adv. Funct. Mater.* **2017**, *27*, 1703140; d) M. Cheng, Y. Jiang, W. Yao, Y. Yuan, R. Deivanayagam, T. Foroozan, Z. Huang, B. Song, R. Rojaee, T. Shokuhfar, Y. Pan, J. Lu, R. Shahbazian-Yassar, *Adv. Mater.* **2018**, *30*, 1800615.
[17] a) P. Zou, Y. Wang, S.-W. Chiang, X. Wang, F. Kang, C. Yang, *Nat. Commun.* **2018**, *9*, 464; b) X.-B. Cheng, R. Zhang, C.-Z. Zhao, Q. Zhang, *Chem. Rev.* **2017**, *117*, 10403.
[18] A. Isogai, T. Saito, H. Fukuzumi, *Nanoscale* **2011**, *3*, 71.
[19] F. M. White, *Fluid Mechanics*, McGraw-Hill, New York **1986**.
[20] S.-Y. Chung, J. T. Bloking, Y.-M. Chiang, *Nat. Mater.* **2002**, *1*, 123.
[21] T. Muraliganth, A. V. Murugan, A. Manthiram, *J. Mater. Chem.* **2008**, *18*, 5661.
[22] M. S. Dresselhaus, A. Jorio, A. G. Souza Filho, R. Saito, *Philos. Trans. R. Soc. A: Math. Phys. Eng. Sci.* **2010**, *368*, 5355.
[23] A. M. Hafez, Y. Jiao, J. Shi, Y. Ma, D. Cao, Y. Liu, H. Zhu, *Adv. Mater.* **2018**, *30*, 1802156.
[24] Y. Li, K. Leung, Y. Qi, *Acc. Chem. Res.* **2016**, *49*, 2363.
[25] J. Cui, T.-G. Zhan, K.-D. Zhang, D. Chen, *Chinese Chem. Lett.* **2017**, *28*, 2171.

